Chinese Chemical Letters 36 (2025) 110027

Contents lists available at ScienceDirect

Chinese Chemical Letters

journal homepage: www.elsevier.com/locate/cclet

Combing NIR-II molecular dye with magnetic nanoparticles for enhanced photothermal theranostics with a 95.6% photothermal conversion efficiency

Xiao-Fang Lv[a], Xiao-Yun Ran[a], Yu Zhao[a], Rui-Rui Zhang[a], Li-Na Zhang[a], Jing Shi[a], Ji-Xuan Xu[b], Qing-Quan Kong[b,*], Xiao-Qi Yu[c], Kun Li[a,*]

[a] Key Laboratory of Green Chemistry Technology, Ministry of Education, College of Chemistry, Sichuan University, Chengdu 610064, China
[b] Hospital of Chengdu Office of People's Government of Tibetan Autonomous Region (Hospital C.T.), Sichuan University, Chengdu 610041, China
[c] Department of Chemistry, Xihua University, Chengdu 610039, China

ARTICLE INFO

Article history:
Received 3 April 2024
Revised 14 May 2024
Accepted 17 May 2024
Available online 19 May 2024

Keywords:
Photothermal therapy
Magnetic nanoparticles
NIR-II fluorescence imaging
Photothermal conversion efficiency
NH_2-Fe_3O_4

ABSTRACT

Photoheranostics have emerged as a promising tool for cancer theranostics owing to their real-time feedback on treatment and their precise diagnosis. Among them, how to improve the photothermal conversion efficiency (PCE) of phototheranostic agents (PTAs) is the key factor for phototheranostic systems. Herein, we provided an efficient method to improve PCE and constructed a biocompatible nano-material ICR-Qu@NH_2-Fe_3O_4@PEG (QNFP) by combing near-infrared second region (NIR-II) molecular dye ICR-Qu and amino-modified magnetic nanoparticles and then encapsulated by DSPE-mPEG2000. QNFP exhibited excellent performance for photothermal therapy with a high PCE of 95.6%. Both *in vitro* and *in vivo* experiments indicated that QNFP could inhibit the growth of tumors under laser irradiation with low toxicity and realized real-time NIR-II fluorescent imaging of tumors. In general, we realized a simple but efficient method to improve the PCE of NIR-II molecular dye without reduce its quantum yield, which is an ideal choice for cancer diagnosis and treatment.

Cancer is still one of the most troublesome and life-threatening diseases people encounter today [1]. Among the various methods for cancer treatment, photothrombotic has gained much recent attention due to its high spatiotemporal selectivity, non-invasive features as well as deep tissue pentation [2-5]. Phototheranostic strategies can make up for the shortcomings of traditional diagnosis and treatment methods [6,7]. Therefore, significant effort has been devoted to developing photothermal materials functional fluorescent including small molecule fluorescent dyes [8-10] and metal nanomaterials [11-13]. These materials absorb the energy of the excitation light that can be converted into thermal energy to be used for photothermal therapy through non-radiation transitions. However, traditional short wavelength photothermal materials only suitable for treatment and diagnosis of superficial lesions owing to its low tissue penetration depth. In recent years, the near-infrared second region (NIR-II) fluorescent dyes are widely used for imaging and treatment because of high tissue penetration and photothermal characteristics, including polymethine cyanine, rhodamine, BODIPY dyes and J-aggregates of molecules [14-17]. Although different NIR-II fluorophores have been reported with widespread use in fluorescence imaging and phototherapy, most of them have low to mild photothermal conversion efficiencys (PCEs). PCE is the key factor of phototheranostic agent for tumor treatment, therefore, how to improve the material's PCE is one of urgent problem to resolve. Researchers are devoted to developing nanomaterials to enhance the PCE by means of self-assembly or nanocomposites. Unfortunately, only few phototheranostics materials with PCE over 90% have been reported yet [18-22].

In the previous study [7], ICR-Qu was developed as a NIR-II phototheranostic agent, which has high PCE and multimodal imaging and therapy. Regrettably, the NIR-II emissions of ICR-Qu was suppressed entirely in water solution and the PCE of ICR-Qu nanoparticles (81.1%) was not satisfactory. Fortunately, not only fluorescent probes but also metal nanomaterials can be used as photothermal agent. For example, Fe_3O_4 nanoparticles can convert absorbed light energy into heat energy under the irradiation of near-infrared light, thus possessing a photothermal effect to some extent [23-25]. As a photothermal agent, the application of Fe_3O_4 nanoparticles has opened up investigations [26-28]. Therefore, it is a superexcellent strategy to achieve the aim of enhancing the

* Corresponding authors.
E-mail addresses: kqqspine@126.com (Q.-Q. Kong), kli@scu.edu.cn (K. Li).

https://doi.org/10.1016/j.cclet.2024.110027
1001-8417/

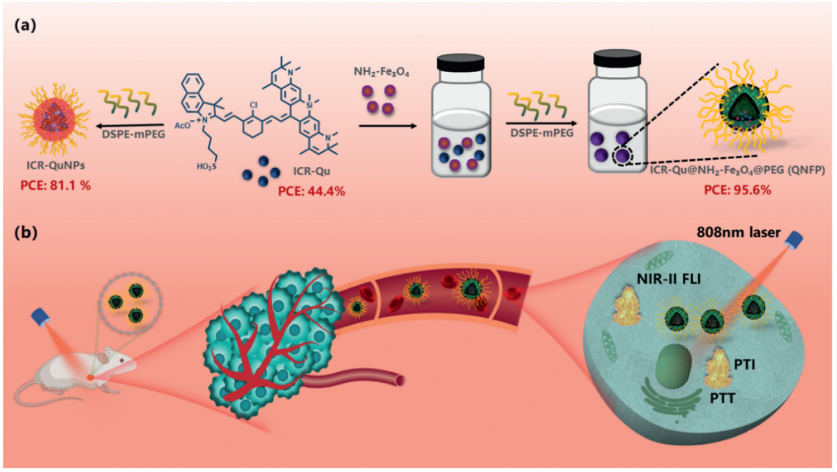

Scheme 1. (a) Schematic illustration of preparation of QNFP. (b) Illustration of the application of QNFP in NIR-II fluorescence imaging (FLI)/photothermal imaging (PTI) and photothermal therapy of cancer.

photothermal effect through preparing a nanocomposite combine NIR-II fluorescent probes and metal nanomaterials with synergistic photothermal characteristics. Inspired by this, herein, we rationally proposed amino-modified magnetic nanoparticles (NH_2-Fe_3O_4) and encapsulated them within ICR-Qu by DSPE-mPEG2000 into nanomaterials (QNFP) (Scheme 1a).

Under 808 nm laser irradiation, QNFP exhibits outstanding NIR-II fluorescence emission and good PCE, which can achieve up to 95.6%. This suggests that QNFP has an efficient photothermal effect and has been successfully applied to image-guided thermal ablation of solid tumors in a mouse model of breast cancer *in vivo*. Overall, QNFP with biocompatibility was successfully performed on photothermal treatment of cancer (Scheme 1b).

The QNFP could be easily achieved *via* simple operation. Firstly, Fe_3O_4 was prepared using the co-precipitation method and then modified with KH-791, which has an amino group to reduce the probability of oxidation and agglomeration. Afterward, ICR-Qu with NIR-II fluorescence characteristics and NH_2-Fe_3O_4 were wrapped by DSPE-mPEG2000 and then the fluorescent-magnetic nanocomposites were obtained. The average hydrodynamic diameter of QNFP was 162 nm (Fig. 1a), and larger than that measured by transmission electron microscopy (Fig. S2 in Supporting information), which may be attributed to the shrinking of the nanoparticles (NPs) during the transmission electron microscope (TEM) sample preparation and the clustering effect of Fe_3O_4 in aqueous condition. These results indicated that the nanocomposites were suitable for tumor labeling due to the enhanced permeability and retention effect (EPR). Besides, we used an X-ray photoelectron spectrometer (XPS) to confirm amino groups were successfully modified on Fe_3O_4 (Fig. S3 in Supporting information). In that, there were characteristic peaks of elements such as N and C in the XPS of NH_2-Fe_3O_4 and the element content of N element was 1%. Although a few, it is enough to suggest that amino groups were successfully modified on the surface of Fe_3O_4. The presence of Fe_3O_4 in QNFP could be further observed in the X-ray diffraction (XRD) result. The characteristic peaks of Fe_3O_4 in the range of 25°–75° could be observed for NH_2-Fe_3O_4 and QNFP as shown in Fig. 1b. These characteristic peaks could be indexed to (220), (311), (400), (511), and (440) planes of the cubic spinel Fe_3O_4 (JCPDS No. 19–0629). As the hysteresis curve (Fig. 1c) showed, the QNFP are superparamagnetic at room temperature with no hysteresis loop and coercivities [29]. To confirm the existence of ICR-Qu onto QNFP, we performed Fourier transform infrared (FT-IR) spectroscopy analysis on the freeze-dried samples. The FT-IR spectra of NH_2-Fe_3O_4,

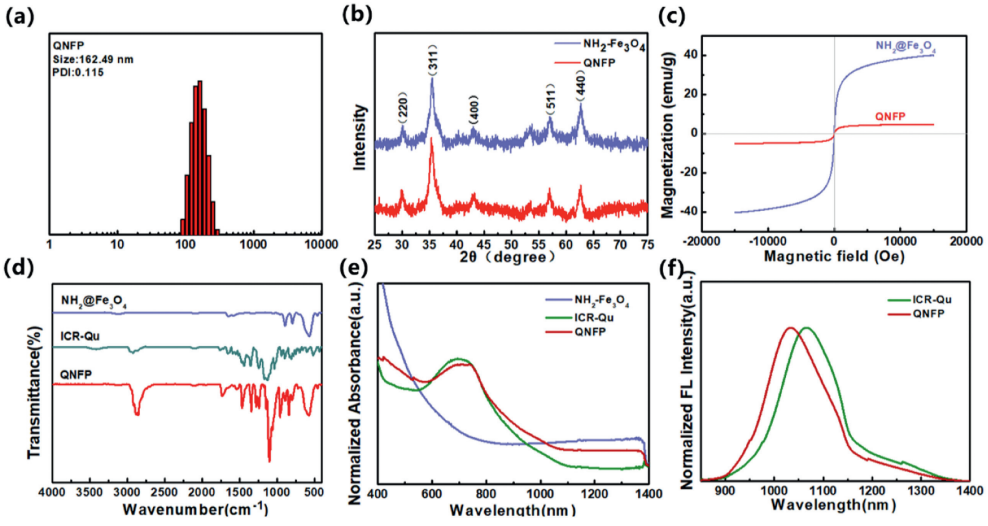

Fig. 1. (a) Particle size measured by DLS of QNFP. (b) XRD patterns of NH_2-Fe_3O_4 and QNFP. (c) Hysteresis loop of NH_2-Fe_3O_4 and QNFP. (d) FT-IR spectra of NH_2-Fe_3O_4, ICR-Qu and QNFP. (e) Normalized absorption spectrum of NH_2-Fe_3O_4, ICR-Qu and QNFP. (f) Normalized FL spectrum of ICR-Qu and QNFP.

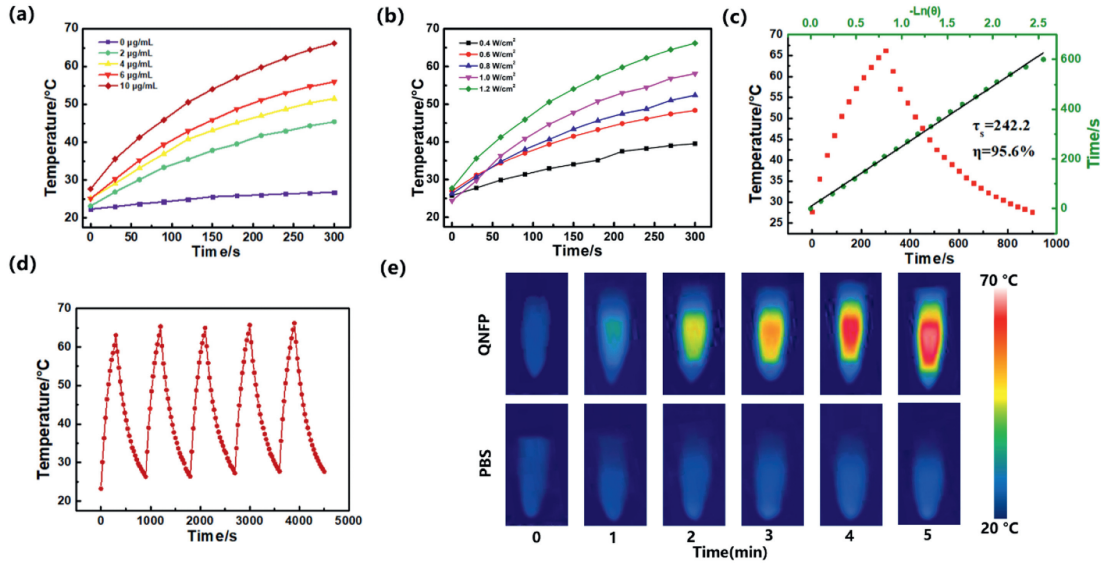

Fig. 2. (a) Concentration–dependent photothermal heating curves of QNFP aqueous solution under 808 nm laser irradiation (1.2 W/cm^2). (b) Power density-dependent photothermal heating curves of QNFP aqueous solution (10 μg/mL) under 808 nm laser irradiation. (c) Photothermal heating and cooling curves of QNFP aqueous solution (10 μg/mL) under 808 nm laser irradiation (1.2 W/cm^2) and linear fitting of cooling time *versus* -ln(θ). (d) Photothermal stability of QNFP under 808 nm laser irradiation (1.2 W/cm^2) for five heating-cooling cycles. (e) Photothermal images of QNFP aqueous solution (10 μg/mL) and PBS buffer under 808 nm laser irradiation (1.2 W/cm^2).

ICR-Qu and QNFP are shown in Fig. 1d. The appearance of the peaks at 1436, 1351, 1249, 1164 cm^{-1} in ICR-Qu and 1460, 1342, 1240, 1101 cm^{-1} in QNFP was ascribed to stretching vibration of aromatic ring. The characteristic peak at 1080 cm^{-1} of QNFP was due to the stretching characteristics of the sulfonic acid group. The characteristic absorption peak at 566 cm^{-1} in NH_2-Fe_3O_4 and 575 cm^{-1} in QNFP was due to the Fe-O stretching. The FT-IR spectrum of QNFP revealed all these characteristic peaks of NH_2-Fe_3O_4, ICR-Qu, confirming the key constitution in the nanocomposites [30,31]. The absorption spectrum of NH_2-Fe_3O_4, ICR-Qu and QNFP and the fluorescence (FL) spectrum of ICR-Qu and QNFP has been shown in Figs. 1e and f. The appearance of the absorption bands at 708 nm and a maximum emission peak around 1030 nm for QNFP confirmed that ICR-Qu has successfully been coated in nanocomposites with an encapsulation efficiency of 57.8%. Furthermore, NH_2-Fe_3O_4 and QNFP exhibited a strong absorption in the NIR wavelength region until 1400 nm, indicating NH_2-Fe_3O_4 has the possibility of convert absorbed light energy into heat energy under the irradiation of near-infrared light. Besides, meanwhile, QNFP showed excellent stability at room temperature (Fig. S4 in Supporting information).

Based on their excellent photophysical property, the photothermal performance of QNFP and NH_2-Fe_3O_4 under 808 nm laser was assessed. As shown in Fig. 2a and Fig. S5a (Supporting information), upon the 808 nm laser irradiation for 5 min (1.2 W/cm^2), the solution of QNFP and NH_2-Fe_3O_4 exhibited a significant concentration dependence and the solution of QNFP dramatically violently warms to 66.2 °C. By contrast, the phosphate buffered saline (PBS) group shows negligible temperature change (<5 °C). What is more, in the same conditions (c = 10 μg/mL), the temperature was warmed by 38.5 °C under 808 nm laser irradiation as the power density increased within 5 min for QNFP in PBS solution, which is much higher than increase of NH_2-Fe_3O_4 (13.7 °C) (Fig. 2b and Fig. S5b in Supporting information). Additionally, because of the synergistic photothermal effect of ICR-Qu and NH_2-Fe_3O_4, the PCE of QNFP was measured (95.6%) and more excellent than NH_2-Fe_3O_4 (52.5%) (Fig. 2c and Fig. S5d in Supporting information), owing to the highest PCE so far compared to nanocomposites that have been reported (Table S1 and Fig. S1 in Supporting information). Notably, the QNFP still had good photostability and photothermal image effect (Figs. 2d and e).

Encouraged by the excellent photothermal properties of QNFP, we then investigated its antitumor performance under 808 nm laser irradiation. As shown in Fig. S6 (Supporting information), more than 90% of 4T1 cells even stayed alive after incubation with 10 μg/mL QNFP for 24 h in the absence of laser; in sharp contrast, the cell viability was no more than 40% with incubation of 10 μg/mL QNFP upon irradiation with 808 nm laser (1.2 W/cm^2) for 5 min. The result indicated that QNFP had tolerable biocompatibility under dark but exhibited high cytotoxicity *via* its photothermal effect under NIR irradiation. Next, to visualize the antitumor efficiency of QNFP under 808 nm laser irradiation, we used the live-dead cell staining analysis with calcein-AM/propidium (PI) to reveal the viability of the 4T1 cells with the QNFP and laser irradiation. The image of confocal laser scanning microscopy (CLSM) (Fig. 3a) showed only the confocal image of 4T1 cells incubated with QNFP exhibited an obvious red emission signal of PI under 808 nm laser irradiation (1.2 W/cm^2) for 5 min, while in other 4T1 cells with treatment of PBS, PBS with laser, or QNFP, only a bright green signal of calcein-AM could be observed. In addition, we also used flow cytometry (FCM) to study the cell death pathways treated by QNFP. The FCM analysis of 4T1 cells with different treatments (Fig. 3b) revealed that after laser irradiation, the percentage of apoptosis cells increased to 42.9% and showed a much higher percentage of apoptosis than that of other groups. This result was similar to CLSM imaging and cell viability assay, which showed that QNFP could induce apoptosis to further cause cell death.

To evaluate the feasibility of QNFP for *in vivo* NIR-II imaging, the distribution in tumors was determined by intravenous injection of QNFP (1.0 mg/kg, 100 μL). The animal experiments were carried out according to the protocol approved by the Ministry of Health in the People's Republic of China and were approved by the Ethical Committees of West China School of Stomatology, Sichuan University (WCHSIRB-D-2017-042). As shown in Figs. 4a and b, the NIR-II fluorescence signal of QNFP at the tumor region was visible after intravenously injecting the NPs for 2 h and then gradually increased with the extension of time. The NIR-II FLI detected the strongest signal of fluorescence after injection at 12 h. Even after 72 h, FL sig-

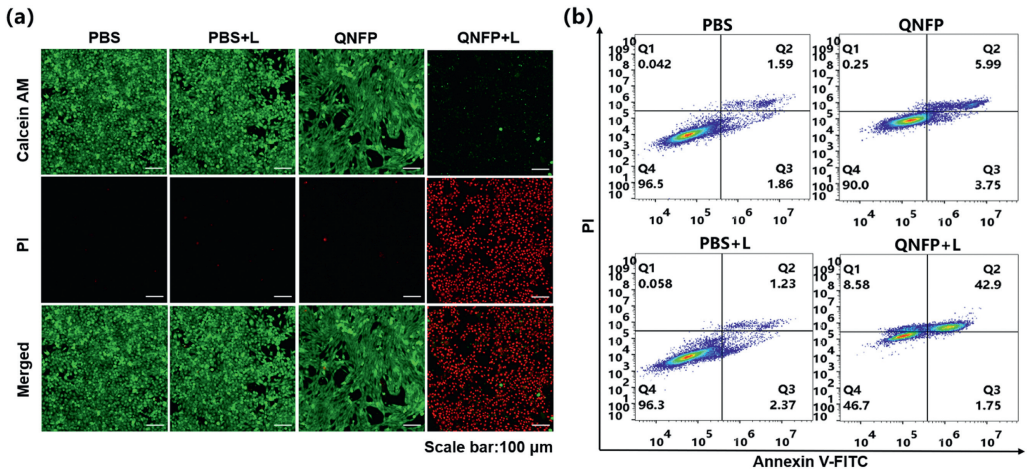

Fig. 3. (a) Confocal images of 4T1 cells with different treatments after being co-stained with calcein-AM (green) and PI (red) for 30 min. (b) Apoptosis analysis by FCM toward 4T1 cells co-stained with Annexin V-FITC/PI dyes after different treatments.

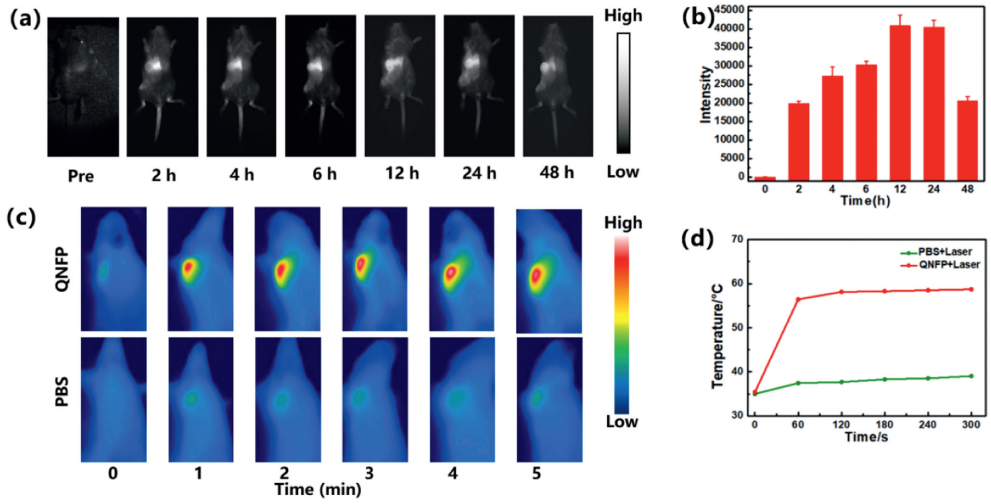

Fig. 4. *In vivo* multimodal imaging of QNFP. (a) NIR-II FLI of 4T1-tumor-bearing BALB/c mice and (b) corresponding fluorescence intensity under 808 nm laser irradiation at different time points after intravenous injection of QNFP (300 μg/mL, 100 μL). (c) NIR-II FLI of 4T1-tumor-bearing BALB/c mice and (d) corresponding fluorescence intensity under 808 nm laser irradiation at different time points after intravenous injection of QNFP (300 μg/mL, 100 μL) with and without magnetic field. Data were presented as mean ± standard deviation (SD) ($n = 5$).

nals could still be observed at the tumor site compared with the major organs (except for liver), which was a sign of their immense potential for tracking tumors in the long term (Fig. S7 in Supporting information). In addition, we investigated the photothermal effect of QNFP in 4T1-tumor-bearing mice after 4 h of the injection of the NPs. With the irradiation of 808 nm laser (0.5 W/cm^2), the temperature of the tumor increased dramatically with increasing irradiation time, reaching 58.7 °C after 5 min. By contrast, it only raised to 39 °C of the control group injected with PBS under the same conditions, indicating that the QNFP represents a promising vehicle to be used in the photothermal therapy (PTT) of subcutaneous tumor-bearing mice (Figs. 4c and d).

Guided by the above results, we further test the PTT effect of QNFP against tumors *in vivo*. The 4T1-tumor-bearing BALB/c mice model was built and then the mice were divided into four groups randomly for different treatments (PBS, PBS + Laser, NPs, NPs + Laser) to value the antitumor effects of different treatment methods. After 3 h of intratumor injection of PBS/NPs, the tumors of the laser groups were irradiated under 808 nm laser (0.5 W/cm^2) for 5 min (Fig. 5a). Infrared thermal imaging, which intuitively showed the temperature changes was used to monitor the temperature variation on the tumor surface in real-time during the laser irradiation periods. The tumor volume and weight of four groups of mice were then monitored for 14 days. After being irradiated with laser, the QNFP + Laser group showed significant inhibition for tumor growth compared with the control groups (PBS, PBS + Laser, and QNFP, Fig. 5b and Fig. S8 in Supporting information). The region of the tumors in the NPs + Laser group showed severe scalding with the irradiation of 808 nm laser, indicating that the 4T1 cells in the group were killed rapidly by hyperthermia generated by QNFP through the photothermal conversion. Furthermore, the mice were sacrificed after 14 days and their tumors were isolated and weighed. As shown in Figs. 5c and d, the tumors in the NPs + Laser group exhibited much lower mean weight and smaller size than that of other groups with significant differences. To verify the 4T1 cell apoptosis, hematoxylin and eosin (H&E) staining and TdT-mediated dUTP nick end labeling (TUNEL) staining were performed. The results are displayed in Figs. 5e and f, showing the obvious damage of tumor tissue and severe cell apoptosis in the NPs + Laser group, while the tumor tissues in the other groups were normal. The above results suggested that QNFP has an excellent PTT effect on subcutaneous tumors in mice. Throughout the

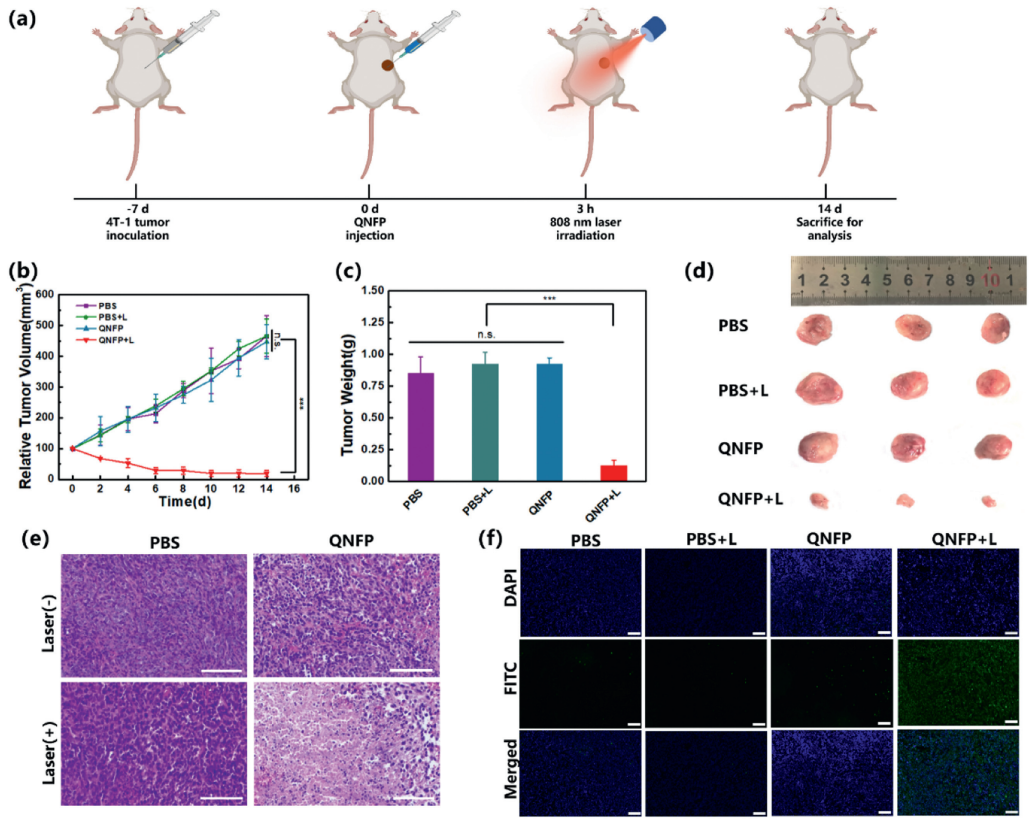

Fig. 5. *In vivo* antitumor performance of QNFP. (a) Schematic diagram of the establishment of 4T1-tumor-bearing BALB/c mice model and QNFP phototherapy. (b) Tumor volume of mice during the treatment period. (c) Weight and (d) digital photographs of tumor after 14 days of treatment. (e) H&E staining analysis of tumor tissues after 14 days of treatment. (f) The tumor TUNEL staining with the different groups. Scale bar: 100 μm. Data were presented as mean ± SD ($n = 3$). n.s., not significant ($P > 0.05$). $^{***}P < 0.001$.

treatment process, the body weight of four groups of mice had no significant differences, indicating that neither the QNFP nor the laser affected the normal growth of the mice (Fig. S9 in Supporting information). Besides, no significant tissue damage was found in the major organs (heart, liver, spleen, lung, and kidney) of the four groups through the H&E staining assay, revealing that the QNFP and laser had no toxicity in various organs (Fig. S10 in Supporting information).

In summary, we have rationally developed a competitive phototheranostic nanocomposite named QNFP by combining NIR-II fluorescent dye (ICR-Qu) and nanoparticles (NH_2-Fe_3O_4). The results suggested that the PCE of ICR-Qu was enhanced obviously by assembly with NH_2-Fe_3O_4 and then encapsulated DSPE-mPEG2000. The PCE of QNFP can reach to 95.6%, which is higher than ICR-Qu (44.4%) and ICR-Qu@PEG (81.1%) because of the trace existence of NH_2-Fe_3O_4. Additionally, both cell validation experiments and *in vivo* tumor treatment experiments proved the excellent photothermal effects of QNFP. Moreover, fluorescence imaging experiments clearly showed that QNFP could capable of labeling tumors of mice by passive transport. Overall, the present method for improving PCE is very helpful for photothermal nanoparticles, which will make these nanocomposites advantageous and efficient for hyperthermal treatment of cancer.

Declaration of competing interest

The authors declare that they have no known competing financial interests or personal relationships that could have appeared to influence the work reported in this paper.

CRediT authorship contribution statement

Xiao-Fang Lv: Writing – original draft, Methodology, Investigation, Formal analysis, Data curation. **Xiao-Yun Ran:** Writing – original draft, Methodology, Conceptualization. **Yu Zhao:** Methodology, Formal analysis. **Rui-Rui Zhang:** Methodology, Investigation. **Li-Na Zhang:** Methodology. **Jing Shi:** Resources. **Ji-Xuan Xu:** Methodology. **Qing-Quan Kong:** Supervision, Funding acquisition. **Xiao-Qi Yu:** Supervision. **Kun Li:** Writing – review & editing, Supervision, Funding acquisition.

Acknowledgments

This work was financially supported by the National Natural Science Foundation of China (Nos. U21A20308, 22077088), Foundation from Science and Technology Major Project of Tibetan Autonomous Region of China (No. XZ202201ZD0001G) and Foundation from Science and Technology Department of Sichuan Province (No. 2021ZHCG0025). We would like to thank the Analytical & Testing Center of Sichuan University for XPS work, and ICP-OES work. We would be grateful to Shuguang Yan for his help with XPS work and Dr. Yani Xie for helping us perform FT-IR studies. The kind assistance of eceshi (www.eceshi.com) for the VSM measurement is greatly appreciated.

Supplementary materials

Supplementary material associated with this article can be found, in the online version, at doi:10.1016/j.cclet.2024.110027.

References

[1] H. Sung, J. Ferlay, R.L. Siegel, et al., CA Cancer J. Clin. 71 (2021) 209–249.
[2] T. Zhang, J. Zhang, F.B. Wang, et al., Adv. Funct. Mater. 32 (2022) 2110526.
[3] Z. Pan, Y. Wang, N. Chen, et al., Bioorg. Chem. 132 (2023) 106349.
[4] H. Shen, C. Xu, R. Ye, et al., Small Sci. 3 (2023) 2300052.
[5] T.T. Wheeler, P. Cao, M.D. Ghouri, et al., Sci. China Chem. 65 (2022) 1498–1514.
[6] Y.Z. Liu, X.Y. Ran, D.H. Zhou, et al., Adv. Funct. Mater. 34 (2023) 2311365.
[7] X.Y. Ran, P. Chen, Y.Z. Liu, et al., Adv. Mater. 35 (2023) 2210179.
[8] Y. Zhang, Q. Shen, Q. Li, et al., Adv. Sci. 8 (2021) 2100386.
[9] W. Cao, Y. Zhu, F. Wu, et al., Small 18 (2022) 2204851.
[10] J. Gao, L. Yuan, Y. Min, et al., Biomater. Sci. 12 (2024) 1320–1331.
[11] Y. Zhang, H. Du, P. He, et al., Sci. China Mater. 64 (2021) 2613–2623.
[12] F. Wei, X. Cui, Z. Wang, et al., Chem. Eng. J. 408 (2021) 127240.
[13] X. Wang, Z. Li, Y. Ding, et al., Chem. Eng. J. 381 (2020) 122693.
[14] J. Mu, M. Xiao, Y. Shi, et al., Angew. Chem. Int. Ed. 61 (2022) e202114722.
[15] B. Zhou, H. Chen, C. Ji, et al., Nanoscale 15 (2023) 17350–17355.
[16] J. Xia, Z. Li, Z. Xie, et al., J. Colloid Interface Sci. 599 (2021) 476–483.
[17] M. Su, Q. Han, X. Yan, et al., ACS Nano 15 (2021) 5032–5042.
[18] Z. Cheng, T. Zhang, W. Wang, et al., Chin. Chem. Lett. 32 (2021) 1580–1585.
[19] X. Xing, P. Zhu, E. Pang, et al., Chin. Chem. Lett. 35 (2024) 109452.
[20] Y. Dai, D. Leng, Z. Guo, et al., Chem. Eng. J. 479 (2024) 147704.
[21] M.M. Zhang, S.L. Chen, A.R. Bao, et al., Angew. Chem. Int. Ed. 63 (2024) e202318628.
[22] Y. Zou, C. Zhang, B. Yang, et al., Plasmonics 18 (2023) 1865–1871.
[23] P. Kharey, S.B. Dutta, M. Manikandan, et al., Nanotechnology 31 (2020) 095705.
[24] J. Hu, H. Wang, F. Dong, et al., Appl. Catal. B: Environ. 204 (2017) 584–592.
[25] G. Guo, T. Zhao, R. Sun, et al., Chin. Chem. Lett. 35 (2024) 109198.
[26] N. Yin, X. Wang, T. Yang, et al., Ceram. Int. 47 (2021) 8271–8278.
[27] Z. Zhang, Q. Wang, L. Han, et al., Sens. Actuators B: Chem. 268 (2018) 188–194.
[28] Y. Jiao, Z. Zhang, K. Wang, et al., Food Chem. X 19 (2023) 100798.
[29] G. Song, M. Kenney, Y.S. Chen, et al., Nat. Biomed. Eng. 4 (2020) 325–334.
[30] P. Xue, M. Hou, L. Sun, et al., Acta Biomater. 81 (2018) 242–255.
[31] W. Guo, Y. Ren, Z. Chen, et al., Adv. Funct. Mater. 33 (2023) 2213921.